

High-Order Small Perturbation Method of Arbitrary Order for Conducting Rough Surface Scattering under TE Incidence

Qing Wang¹, Chen Lin², Zhen-Ya Lei¹, Jianq-Qiang Hou¹, and Lei Li¹

¹School of Electronic Engineering
Xidian University, Xi'an, Shaanxi 710071, China
wangqing@mail.xidian.edu.cn, zylei@xidian.edu.cn, jqhou@mail.xidian.edu.cn, leili@mail.xidian.edu.cn

²Second Research Department
Yangzhou Marine Electronic Institute, Yangzhou, Jiangsu 225001, China
xidianlc@163.com

Abstract — A novel closed-form high-order small perturbation method (HOSPM) for the analysis of scattering from 1-D conducting random rough surfaces under TE incidence is developed. The main theoretical contributions of the HOSPM are as follows: (1) our method yields a general high-order SPM form for scattered fields of arbitrary orders, (2) Faà di Bruno's formula is introduced into computational electromagnetics (CEM) for the first time to expand a tapered incident wave and its partial derivatives in power series form, and (3) the form is simple and easy to program and does not require any mathematical pretreatment. Comparisons are made between the method of moments (MOM) and different-order HOSPMs in terms of several aspects, including accuracy and time efficiency. The order convergence of the HOSPM is discussed, the regions of validity with regard to correlation lengths and root mean square (RMS) heights are demonstrated for the 2nd-order HOSPM, and the robustness of the 2nd-order HOSPM is proven over a broad range of frequencies.

Index Terms — Bistatic scattering coefficients, high-order small perturbation method, rough surface scattering, tapered wave, TE incidence.

I. INTRODUCTION

The scattering of EM waves from a random rough surface has been an important subject of research in recent decades because of its important applications in many diverse fields, including electromagnetic scattering [1-3], remote sensing [4], oceanography [5], communications [6], materials science [7-8], medical imaging [9] and applied optics [10-11]. Methods of studying rough surface scattering can be categorized into three groups: (1) approximation and analytical methods, (2) numerical methods and (3) semi-analytical methods. Approximation methods are based on physical

approximations and are aimed at providing closed-form formulae for the scattered fields. The basic idea of numerical methods is to discretize the continuous variable and continuous functions, convert the differential equations into the difference equations, convert the integral equations to the form of finite sum, establish the convergent algebraic equations, and use the computer technology to solve the problem. Semi-analytical methods are a combination of numerical methods and analytical methods. The main principle of the semi-analytical methods is to reduce the dimension of multidimensional problems by using the family of low-dimensional solutions so as to simplify the calculation.

The small perturbation method (SPM) is a classic approximation method for rough surface with small-scale roughness [12-14]. The SPM produces a series expansion in the surface heights for a scattered field. There are two classic approaches to the SPM. The first one is based on the extended boundary condition (EBC) method. The surface currents on the rough surface are first calculated by applying the extinction theorem. The scattered fields can then be calculated from the diffraction integrals of the surface fields. The second approach makes use of the Rayleigh hypothesis to express the reflected and transmitted fields as upward- and downward-going waves, respectively. The field amplitudes are then determined from the boundary conditions [15]. Both perturbation methods yield the same expansion for the scattered fields.

There have been many quantitative studies aimed at analysis and applications of different-order SPMs. The first-order SPM has been used to predict scattering from multilayer stacks, especially light scattering from multilayer optical coatings [16-17]. The Born-approximation first-order SPM is frequently applied to high-frequency scattering from marine sediments [18]. In the original paper [19], scattered fields of up to second order in surface height were considered for scattering

from 2-D random rough surfaces. In [20], scattered fields were derived to third order in the surface height, and expressions for the scattered and transmitted powers were developed for deterministic and stochastic surfaces as well as periodic and nonperiodic surfaces. The fourth-order SPM was investigated with regard to scattering from two rough surfaces in a layered geometry in [21].

Most SPM studies can only supply solutions in the form of limited series. Usually, as series order increases, the integral dimensionality increases. The necessary calculations are complicated to code when they involve multiple integrals. Because high-order mathematical forms are always complex and difficult to program, there is no general form for an SPM of arbitrary orders. In order to solve these problems, this paper presents a semi-analytical version of the SPM for arbitrary orders, such that the highest order of the method can even be infinite. Therefore, the proposed method is called the high-order SPM (HOSPM). In this method, a tapered incident wave is used to avoid “edge diffraction”. Because the incident wave should also be expanded in series form, another new consideration in the HOSPM is the introduction of Faà di Bruno's formula to expand a tapered incident wave and its partial derivatives in power series form. This is the first time that Faà di Bruno's formula has been used in CEM.

There are several differences between the classic SPM and our method. (1) The classic SPM makes use of the Rayleigh hypothesis. Our method is based on the Ewald-Oseen extinction theorem [22]. (2) Although both methods use Taylor series to expand the scattered and incident fields, the spectral amplitude inside the Fourier transform is expanded in series form in the classic SPM, whereas the total field is expanded into a Taylor series in our method. (3) In the classic SPM, the scattered fields are classified as either coherent or incoherent waves. In our method, this classification is not needed, and the scattered fields are calculated from the diffraction integrals of the total surface fields. (4) In the classic SPM, the Fourier coefficients are determined via multi-integrals, and the integral dimensionality increases as the order of the terms increases. Our method involves only 1-D integrals regardless of the order and thus is simpler to express in mathematical form and much easier to code. (5) Edge diffraction is not considered in the classic SPM, whereas our method considers tapered waves to eliminate edge diffraction.

The HOSPM is based on the assumption that the boundary conditions are perturbed around those of a smooth surface. To verify the validity of the HOSPM, its solution should be compared with a solution obtained without imposing any restriction on the rough-surface properties. Numerical methods are most suitable for this purpose. One of the most widely used numerical methods is the method of moments (MOM). Therefore,

the MOM is chosen as the comparison method in this study to enable a more conclusive analysis. Simulations performed on 1-D one-layer conducting random rough surfaces with a Gaussian height distribution are reported. Such surfaces are the simplest to describe statistically and can be fully characterized by the surface correlation function. The Thorsos tapered wave [23] is chosen here for its accuracy and broad applications in the truncation of rough surfaces.

The paper is organized as follows. Section II gives the preliminaries. Section III presents all functions involved in the derivation of the HOSPM. In Section IV, many aspects of the HOSPM are analyzed, including accuracy, convergence, time efficiency, memory consumption, the influences of different correlation lengths and root mean square (RMS) heights, and frequency robustness. The conclusion is presented in Section V.

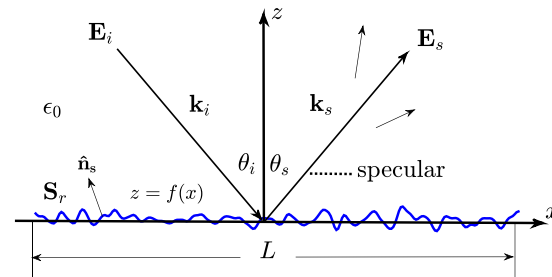


Fig. 1. Geometry for wave scattering by a conducting random rough surface.

II. PRELIMINARIES

The model under investigation is the 1-D conducting random rough surface shown in Fig. 1, and a two-dimensional scattering problem is considered. The analysis is conducted in the frequency domain, with the time-dependence factor $e^{-i\omega t}$ omitted throughout. The case of interest is the TE case, so the electric field has the form:

$$\mathbf{E} = \mathbf{y}\psi, \quad (1)$$

where ψ is the quantity of the electric field. Throughout the remainder of the paper, the scalar wave equation ψ is studied instead of \mathbf{E} for simplicity.

Because the wave equation ψ is scalar, the scalar Green's Theorem is used, which has the form:

$$\begin{aligned} & \iint_V dv [\psi(\mathbf{r})\nabla^2 g(\mathbf{r},\mathbf{r}') - g(\mathbf{r},\mathbf{r}')\nabla^2 \psi(\mathbf{r})] \\ & = \oint_S d\mathbf{S} \cdot [\psi(\mathbf{r})\nabla g(\mathbf{r},\mathbf{r}') - g(\mathbf{r},\mathbf{r}')\nabla \psi(\mathbf{r})], \end{aligned} \quad (2)$$

where $g(\mathbf{r},\mathbf{r}')$ is the Green's function; \mathbf{S} is the closed surface composed of the rough surface \mathbf{S}_r (shown in Fig. 1) and the half-circle \mathbf{S}_i , with a radius extending to

infinity; \mathbf{r}' is above the surface \mathbf{S}_r ; and \mathbf{r} is on the surface \mathbf{S}_r .

Upon the application of the extinction theorem [24], supposing that the surface is perfectly conducting and employing the Dirichlet boundary condition $\psi(\mathbf{r}) = 0$ for \mathbf{r} on \mathbf{S}_r , the expression for the scattered field should be:

$$\begin{aligned} \psi_s(\mathbf{r}') &= \int_{\mathbf{S}_r} d\mathbf{s} \mathbf{n}_s \cdot [-g(\mathbf{r}, \mathbf{r}') \nabla \psi(\mathbf{r})] \\ &= - \int_{\mathbf{S}_r} ds g(\mathbf{r}, \mathbf{r}') [\mathbf{n}_s \cdot \nabla \psi(\mathbf{r})] \\ &= - \int_{-L/2}^{L/2} dx g(\mathbf{r}, \mathbf{r}') \sqrt{1 + \left(\frac{df}{dx}\right)^2} \frac{\partial \psi(\mathbf{r})}{\partial n_s}, \end{aligned} \quad (3)$$

where \mathbf{r}' is located in the upper space; $z = f(x)$ is the surface height profile of the rough surface, with the spectral density function $W(k)$; and \mathbf{n}_s is the unit normal vector of the rough surface pointing toward the upper space.

To prevent current discontinuity at the end points [24], we can use either a tapered incident wave or periodic boundary conditions [25-27]. Because the rough interface modeled in the simulation is of finite size, a tapered incident wave is used. The Thorsos tapered wave has been extensively applied for this purpose because of its low computational expense. The form of the tapered incident wave is as follows:

$$\psi_i(\mathbf{r}) = e^{ik(x \sin \theta_i - z \cos \theta_i) [1 + w(\mathbf{r})] - \frac{(x+z \tan \theta_i)^2}{g^2}}, \quad (4)$$

with

$$w(\mathbf{r}) = \frac{2(x + z \tan \theta_i)^2 / g^2 - 1}{(kg \cos \theta_i)^2}, \quad (5)$$

where k is the wave number of free space, θ_i is the incidence angle, and g is the tapering parameter.

III. FORMULATION

A. Solutions for the total and scattered fields

Because its variable has the form $\mathbf{r} = x\mathbf{x} + f(x)\hat{\mathbf{z}}$, the field $\psi(\mathbf{r})$ on the random rough surface is related to the profile of the scattering surface $f(x)$. In the case of a slightly rough surface, the RMS height h of the surface is far smaller than both the incident wavelength λ and the absolute value of $f(x)$. According to the power series expansion theory, which is valid when the variable (in our case, the absolute value of the height profile, $|f(x)|$) is small, the field on the rough surface can be expanded as a Taylor series about the field on the mean surface ($z = f(x) = 0$):

$$\begin{aligned} \psi(\mathbf{r}) &= \sum_{m=0}^n \frac{f^m}{m!} \frac{\partial^m \psi}{\partial z^m} \Big|_{z=0} \\ &= \psi \Big|_{z=0} + f \frac{\partial \psi}{\partial z} \Big|_{z=0} + \frac{f^2}{2!} \frac{\partial^2 \psi}{\partial z^2} \Big|_{z=0} + \frac{f^3}{3!} \frac{\partial^3 \psi}{\partial z^3} \Big|_{z=0} \\ &\quad + \frac{f^n}{n!} \frac{\partial^n \psi}{\partial z^n} \Big|_{z=0}, \end{aligned} \quad (6)$$

where ψ and f on the right are used in place of $\psi(\mathbf{r})$ and $f(x)$ for brevity. In this equation, n can theoretically approach infinity. $\psi(\mathbf{r})$ is composed of an incident field and a scattered field. The certain part of $\psi(\mathbf{r})$ is the incident field, and the uncertain part is determined by the scattered field. The scattered field on the rough space as well as the total field can be expressed as the sum of the zeroth-order field component, the first-order field component, and all other components up through the n th-order field component, as follows:

$$\psi_s(\mathbf{r}) = \sum_{m=0}^n \psi_m^s(\mathbf{r}). \quad (7)$$

Based on equations (6) and (7), the different-order series expressions for the total field on the surface should be as follows:

$$\psi_0(\mathbf{r}) = \psi_i \Big|_{z=0} + \psi_0^s \Big|_{z=0}, \quad (8.0)$$

$$\begin{aligned} \psi_1(\mathbf{r}) &= \psi_i \Big|_{z=0} + \psi_0^s \Big|_{z=0} + \psi_1^s \Big|_{z=0} + f \frac{\partial}{\partial z} (\psi_i + \psi_0^s) \Big|_{z=0}, \end{aligned} \quad (8.1)$$

$$\begin{aligned} \psi_2(\mathbf{r}) &= \psi_i \Big|_{z=0} + \psi_0^s \Big|_{z=0} + \psi_1^s \Big|_{z=0} + \psi_2^s \Big|_{z=0} \\ &\quad + f \frac{\partial}{\partial z} (\psi_i + \psi_0^s + \psi_1^s) \Big|_{z=0} + \frac{f^2}{2} \frac{\partial^2}{\partial z^2} (\psi_i + \psi_0^s) \Big|_{z=0}, \end{aligned} \quad (8.2)$$

⋮

$$\psi_n(\mathbf{r}) = \sum_{m=0}^n \frac{f^m}{m!} \cdot \frac{\partial^m}{\partial z^m} \left(\psi_i + \sum_{l=0}^{n-m} \psi_l^s \right) \Big|_{z=0}, \quad (8.n)$$

where ψ_i , ψ_0^s , ψ_1^s , ... and ψ_n^s are used as abbreviations for $\psi_i(\mathbf{r})$, $\psi_0^s(\mathbf{r})$, $\psi_1^s(\mathbf{r})$, ... and $\psi_n^s(\mathbf{r})$, respectively. Based on equation (8.n), the partial derivatives of $\psi_n(\mathbf{r})$ with respect to x and z should be:

$$\frac{\partial \psi_n(\mathbf{r})}{\partial x} = \sum_{m=1}^{n+1} \frac{f^{m-1}}{(m-1)!} \frac{\partial^{m-1}}{\partial z^{m-1}} \left(\frac{\partial \psi_i}{\partial x} + \sum_{l=0}^{n-m+1} \frac{\partial \psi_l^s}{\partial x} \right) \Big|_{z=0}, \quad (9)$$

$$\frac{\partial \psi_n(\mathbf{r})}{\partial z} = \sum_{m=1}^n \frac{f^{m-1}}{(m-1)!} \frac{\partial^m}{\partial z^m} \left(\psi_i + \sum_{l=0}^{n-m} \psi_l^s \right) \Big|_{z=0}. \quad (10)$$

Because equations (8.0) to (8.n) represent total field expressions of different orders, each of them should obey the same boundary condition at the interface. By

simultaneously applying the Dirichlet boundary condition to equations (8.0) ~ (8.*n*), the 0th-order through *n*th-order expressions for the scattered field on the mean surface $z=0$ can be obtained as follows:

$$\psi_0^s(\mathbf{r})\Big|_{z=0} = -\psi_i\Big|_{z=0}, \quad (11.0)$$

$$\psi_1^s(\mathbf{r})\Big|_{z=0} = -f \frac{\partial(\psi_i + \psi_0^s)}{\partial z}\Big|_{z=0}, \quad (11.1)$$

$$\psi_2^s(\mathbf{r})\Big|_{z=0} = -f \frac{\partial\psi_1^s}{\partial z}\Big|_{z=0} - \frac{f^2}{2!} \frac{\partial^2(\psi_0^s + \psi_i)}{\partial z^2}\Big|_{z=0}, \quad (11.2)$$

$$\vdots$$

$$\psi_n^s(\mathbf{r})\Big|_{z=0} = -\frac{f^n}{n!} \frac{\partial^n \psi_i}{\partial z^n}\Big|_{z=0} - \sum_{m=1}^n \frac{f^m}{m!} \frac{\partial^m \psi_{n-m}^s}{\partial z^m}\Big|_{z=0}. \quad (11.n)$$

To obtain the *n*th-order partial derivatives of the scattered field on the rough surface $\psi_n^s(\mathbf{r})$, the spectral domain integral is used as follows:

$$\psi_n^s(\mathbf{r}) = \int_{-\infty}^{\infty} dk_x A_n(k_x) e^{i[k_x x + k_z f(x)]}, \quad (12)$$

where $k_z = \sqrt{k^2 - k_x^2}$. In this way, the scattered field is expressed in the space domain as an accumulated spectrum of waves with different propagation directions and different amplitudes. $A_n(k_x)$ is the amplitude of each wave in the spectrum. The following relationships are obtained on the mean surface:

$$\psi_n^s(\mathbf{r})\Big|_{z=0} = \int_{-\infty}^{\infty} dk_x A_n(k_x) e^{ik_x x}, \quad (13)$$

$$A_n(k_x) = \frac{1}{2\pi} \int_{-\infty}^{\infty} dx \left[\psi_n^s(\mathbf{r})\Big|_{z=0} \right] e^{-ik_x x}, \quad (14)$$

$$\frac{\partial^m \psi_n^s(\mathbf{r})}{\partial z^m}\Big|_{z=0} = i^m \int_{-\infty}^{\infty} dk_x k_x^m A_n(k_x) e^{ik_x x}, \quad (15)$$

$$\frac{\partial \psi_n^s(\mathbf{r})}{\partial x}\Big|_{z=0} = i \int_{-\infty}^{\infty} dk_x k_x A_n(k_x) e^{ik_x x}, \quad (16)$$

$$\frac{\partial^m}{\partial z^m} \left(\frac{\partial \psi_n^s(\mathbf{r})}{\partial x} \right)\Big|_{z=0} = i^{m+1} \int_{-\infty}^{\infty} dk_x k_x k_x^m A_n(k_x) e^{ik_x x}. \quad (17)$$

By calculating the Fourier transform of equation (14), $A_n(k_x)$ is determined. The amplitude is substituted into equations (15), (16) and (17), and the inverse Fourier transforms are applied subsequently. Accordingly, the partial derivative terms $\left[\frac{\partial^m \psi_n^s(\mathbf{r})}{\partial z^m} \right]\Big|_{z=0}$, $\left[\frac{\partial \psi_n^s(\mathbf{r})}{\partial x} \right]\Big|_{z=0}$ and $\left\{ \frac{\partial^m}{\partial z^m} \left[\frac{\partial \psi_n^s(\mathbf{r})}{\partial x} \right] \right\}\Big|_{z=0}$ can

be determined. These partial derivative terms are needed in the calculation of equations (8.0) ~ (8.*n*), (9) and (10). The partial derivatives of the tapered incident field are derived in Appendix.

B. Bistatic scattering coefficients

As expressed in equation (3), the scattered field in the upper space can be obtained by integrating the Green's function with the directional derivative of the total field at the interface \mathbf{S}_r . The two-dimensional Green's function in equation (3) is:

$$g(\mathbf{r}, \mathbf{r}') = \frac{i}{4} H_0^{(1)}(k|\mathbf{r} - \mathbf{r}'|). \quad (18)$$

When this Green's function is expanded at infinity, the Hankel function $H_0^{(1)}(k|\mathbf{r} - \mathbf{r}'|)$ can be approximated as follows when \mathbf{r}' is located at an infinitely far distance and the observation is in the direction of $\mathbf{k}_s = \sin \theta_s \mathbf{x} + \cos \theta_s \mathbf{z}$:

$$H_0^{(1)}(k|\mathbf{r} - \mathbf{r}'|) \approx \sqrt{\frac{2}{\pi k|\mathbf{r} - \mathbf{r}'|}} e^{i(k|\mathbf{r} - \mathbf{r}'| - \frac{\pi}{4})}$$

$$\approx \sqrt{\frac{2}{\pi k r'}} e^{ikr'} e^{-i\frac{\pi}{4}} e^{-ik[x \sin \theta_s + f(x) \cos \theta_s]}. \quad (19)$$

Upon substituting equations (18) and (19) into equation (3) and setting the total field to be of *n*th-order, the scattered fields can be written as:

$$\psi_s(\mathbf{r}') = -\frac{i}{4} \sqrt{\frac{2}{\pi k r'}} e^{-i\frac{\pi}{4}} e^{ikr'} \psi_n^{N_s}(\theta_s), \quad (20)$$

with

$$\psi_n^{N_s}(\theta_s) = \int_{-L/2}^{L/2} dx e^{-ik[x \sin \theta_s + f(x) \cos \theta_s]} \sqrt{1 + \left(\frac{df}{dx} \right)^2} \frac{\partial \psi_n(\mathbf{r})}{\partial n_s}, \quad (21)$$

where

$$\frac{\partial \psi_n(\mathbf{r})}{\partial n_s} = \nabla \psi_n(\mathbf{r}) \cdot \mathbf{n}_s, \quad (22)$$

and

$$\mathbf{n}_s = \frac{-\frac{df}{dx} \hat{x} + \hat{z}}{\sqrt{1 + \left(\frac{df}{dx} \right)^2}}. \quad (23)$$

Consequently,

$$\psi_n^{N_s}(\theta_s) = \int_{-L/2}^{L/2} dx e^{-ik[x \sin \theta_s + f(x) \cos \theta_s]} \left[-\frac{df}{dx} \frac{\partial \psi_n(\mathbf{r})}{\partial x} + \frac{\partial \psi_n(\mathbf{r})}{\partial z} \right], \quad (24)$$

where $\frac{\partial \psi_n(\mathbf{r})}{\partial x}$ and $\frac{\partial \psi_n(\mathbf{r})}{\partial z}$ can be obtained from equations (9) and (10).

The expression for the normalized far-field bistatic scattering coefficients (BSCs) is [24]:

$$\begin{aligned} \sigma_n(\theta_i, \theta_s) &= \frac{r'S_s(\mathbf{r}')}{-\int_{-\infty}^{\infty} dx \left(S_{inc} \cdot \hat{\mathbf{z}} \right)_{z=0}} \\ &= \frac{-\frac{1}{2\eta k} \text{Im} \left[\psi_n^s(\mathbf{r}') \nabla \psi_n^{s*}(\mathbf{r}') \right]}{P_{inc}}. \end{aligned} \quad (25)$$

For a plane wave, $\mathbf{S}_{inc} \cdot \hat{\mathbf{z}} = -\cos \theta_i / (2\eta)$, and η is the intrinsic impedance of free space. Accordingly, the power P_{inc} received by the rough surface should be:

$$P_{inc} = -\int_{-\infty}^{\infty} dx \left(\mathbf{S}_{incp} \cdot \hat{\mathbf{z}} \right)_{z=0} = -\int_{-\infty}^{\infty} dx \frac{1}{2\eta} \cos \theta_i. \quad (26)$$

The value of the quantity expressed in equation (26) approaches infinity. This makes the calculation of $\sigma_n(\theta_i, \theta_s)$ impossible. However, this dilemma can be resolved by using the Thorsos tapered wave as the incident wave[23]. In this case,

$$\begin{aligned} \sigma_{n(\text{tapered wave})}(\theta_i, \theta_s) &= \frac{\frac{1}{2\eta} \frac{1}{8\pi k} \left| \psi_n^{N_s}(\theta_s) \right|^2}{P_{inc(\text{tapered wave})}} \\ &= \frac{\left| \psi_n^{N_s}(\theta_s) \right|^2}{8\pi k g \sqrt{\frac{\pi}{2}} \cos \theta_i \left[1 - \frac{1 + 2 \tan^2 \theta_i}{2k^2 g^2 \cos^2 \theta_i} \right]}, \end{aligned} \quad (27)$$

where

$$P_{inc(\text{tapered wave})} = \frac{\cos \theta_i}{2\eta} g \sqrt{\frac{\pi}{2}} \left(1 - \frac{1 + 2 \tan^2 \theta_i}{2k^2 g^2 \cos^2 \theta_i} \right). \quad (28)$$

The BSCs can then be determined using equation (27) and the related equations above.

C. Monte Carlo simulation

To obtain the statistical averages of the BSCs for random rough surfaces, Monte Carlo simulations are used. In the simulation process, independent samples of rough surfaces are first generated, and the BSCs for each sample are individually computed. Then, the statistical averages of the BSCs for m independent computations are determined as follows:

$$\bar{\sigma}^m = \left[\sigma^m + \bar{\sigma}^{m-1} \cdot (m-1) \right] / m, \quad (29)$$

where m ($1 \leq m \leq M$) is the index representing the number of computations, M is the total number of surface realizations, $\bar{\sigma}^m$ is the statistical average, and σ^m is the value from the m th simulation.

IV. VALIDATION

In this section, several numerical examples are presented to evaluate the HOSPM in terms of many

aspects, including accuracy, convergency, time efficiency, the influences of correlation lengths and RMS heights, and frequency robustness. Because of its wide range of accuracy [28], the MOM is employed as the method for comparison. The general formulation of the MOM is described in [24], and all code for implementing the MOM is based on Dr. Tsang Leung's Electromagnetic Wave MATLAB Library. Because this paper considers a 1-D problem under TE incidence, all simulations default to HH polarization. To fully exploit the computational efficiency of FFT operations, the number of points on the rough surface is set to be a power of two.

A. Accuracy and convergency

A table and a figure are presented in this subsection. Because subsection D addresses the influences of frequency, a fixed wavelength of $\lambda = 1\text{m}$ is considered in subsection A, B and C. All of the parameters used to generated the results shown in Fig. 2 are listed in the figure, including the rough surface length L , the RMS height h , the correlation length l , the tapering parameter g , the incidence angle θ_i , the number of points N on the surface and the number of iterations (samples) M ; these are also the parameters used for the simulations reported in Table 1.

Table 1: The accuracy of HOSPM on backscattering and forward scattering direction and relative errors between different orders

n	$\Delta_b(\text{dB})$	$\Delta_s(\text{dB})$	Σ_n
1	0.59	0.40	/
2	0.23	0.41	0.027
3	0.24	0.39	0.049
4	0.24	0.39	1.90×10^{-7}
5	0.24	0.39	1.28×10^{-5}
6	0.24	0.39	1.13×10^{-7}
7	0.24	0.39	1.15×10^{-8}
8	0.24	0.39	1.75×10^{-11}

n : order of HOSPM.

Δ_b : $|\sigma_n(\text{MOM}) - \sigma_n(\text{HOSPM})|$ in the backscattering angle.

Δ_s : $|\sigma_n(\text{MOM}) - \sigma_n(\text{HOSPM})|$ in the forward scattering angle.

Σ_n : relative error for the n th-order HOSPM.

Figure 2 shows the BSCs for 1-D perfectly electrically conducting (PEC) Gaussian random rough surfaces obtained using different-order HOSPMs and the MOM. In the figure, the curves obtained using the 1st-, 2nd-, 4th- and 8th-order HOSPMs do not show significant differences. The curve of MOM and the curves from HOSPMs match well to the left of the specular scattering point. The value of BSCs generally coincide between the HOSPMs and the MOM over

a wide range of scattering angles from precisely -89° to 41° . As can be seen from Fig. 2 in the manuscript, the BSCs generally coincide between the HOSPMs and the MOM over a wide range of scattering angles from approximately -89° to 41° , with good matching for many angles.

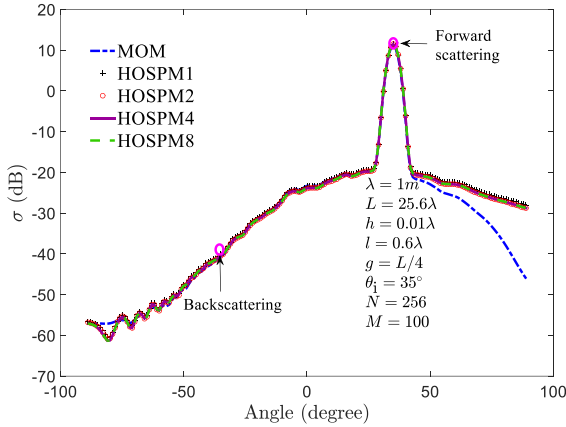


Fig. 2. Comparisons of the BSCs by 1st-order, 2nd-order, 4th-order and 8th-order HOSPM and MOM.

The biggest difference between the two methods lies in how to get the value of the term

$$\left[-\frac{df}{dx} \frac{\partial \psi_n(\mathbf{r})}{\partial x} + \frac{\partial \psi_n(\mathbf{r})}{\partial z} \right]$$
 in the integrand in Eq. (21).

MOM uses a numerical method which is solving the matrix, and HOSPM uses the method which is a series of formulas related to the series expansion. Therefore, the final values obtained by the two methods are difficult to be exactly the same, which is the main reason why the matching between HOSPM and MOM is not good for angle larger than 41° .

For more specific investigations, two representative angles, the backscattering angle and the forward scattering angle, are selected as objects of study. These two angles are also of the greatest interest compared with other angles.

Table 1 presents the results for the precision of the different-order HOSPMs in the backscattering and forward scattering directions and the convergence among the different-order HOSPMs. Comparisons of precision between n th-order HOSPMs and the MOM in the backscattering and forward scattering directions are given in the second and third rows of Table 1. At 1st order and above, the HOSPM shows high precision, with differences of less than 0.6 dB between the two methods.

Since HOSPM are expressed in the form of series

of arbitrary orders, the order convergence should be discussed. The fourth row in Table 1 shows the iteration errors from the 2nd-order to the 8th-order HOSPM.

The relative errors for BSCs of different orders that are reported in the fourth row of Table 1 are denoted by Σ_n and are defined as:

$$\Sigma_n = \max \left| \frac{\sigma_n(\theta_i) - \sigma_{n-1}(\theta_i)}{\sigma_{n-1}(\theta_i)} \right|, (n \gg 2). \quad (30)$$

As seen from Table 1, the relative error Σ_n decreases as the order n increases. If we set 5% as the threshold for convergence, the values obtained for the 1st-order HOSPM and above are acceptable. Because the relative errors of the 2rd-order HOSPM and above are negligible, the terms of 2rd-order and above in the series can be ignored, consistent with the error property of power series.

These findings prove that our method is accurate and stable. Considering both the accuracy and convergence results, the BSCs obtained using the 1st-order HOSPM and above can be considered acceptable.

B. Time and memory consumption

Without the application of any acceleration algorithms, the MOM has a memory requirement of $O(N^2)$ and a computational complexity of $O(N^3)$, where N is the total number of sample points per interface. A precise analysis reveals that, the HOSPM requires $O[(n+1)N]$ memory and $O[(n+1)!n^3N]$ operations. Therefore, the HOSPM is theoretically superior to the MOM in both memory and complexity because of $n \ll N$. The HOSPM also exhibits computational advantages in practice, as shown in Table 2 and Fig. 3. Table 2 presents the time consumption data for the MOM and for the 2nd-, 3rd- and 4th-order HOSPMs, which vary with the number of points on the surface.

Table 2: The time cost by MOM and HOSPM of different orders (s)

N	2^8	2^9	2^{10}	2^{11}	2^{12}	2^{13}
t	2.13	6.51	25.13	103.70	491.51	2532.0
t_1	1.69	2.97	5.75	11.50	27.57	74.48
t_2	4.61	8.44	16.61	35.83	87.56	238.2
t_3	10.56	19.55	39.10	85.33	208.91	579.47
t_4	22.68	41.81	85.62	186.47	458.19	1239.8

t : the time cost by MOM.

t_1 : the time cost by HOSPM1.

t_2 : the time cost by HOSPM2.

t_3 : the time cost by HOSPM3.

t_4 : the time cost by HOSPM4.

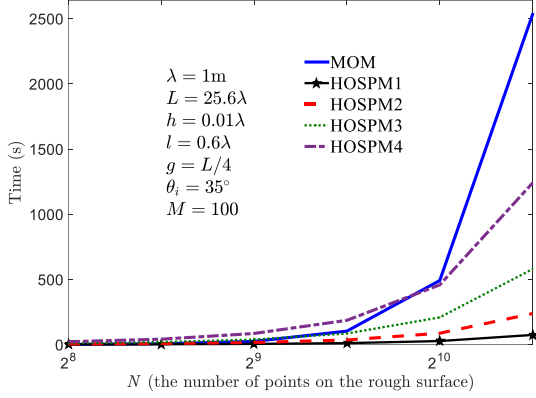


Fig. 3. Time cost by MOM and HOSPMs with 1st-, 2nd-, 3rd- and 4th-order (in the unit of second).

Figure 3 illustrates the data summarized in Table 2. The parameters used to generate the results presented in Fig. 3 and Table 2 are listed in the figure. Among the different-order HOSPMs, the 1st-order method exhibits the best time performance. Its time curve is nearly linear, whereas the MOM has a quadratic cubic time curve. As the order of the HOSPM increases, the curve becomes steeper, indicating worse efficiency. However, even the 4th-order HOSPM still shows better efficiency compared with the MOM when the number of points is greater than 2^{12} . Because of the use of FFT operations, the value of N must have the form 2^{N_1} , where N_1 is an integer. When $N_1=10$, the 1st- and 2nd-order HOSPM shows better time performance than the MOM; when $N_1=11$, the 1st-, 2nd- and 3rd-order HOSPMs perform better; and when $N_1=13$, the HOSPMs all perform better. Thus, we can conclude that our method shows good potential in terms of time efficiency for electrically large surfaces.

Considering the time efficiency, the 1st-order HOSPM is the best choice. Considering all the factor discussed above (the time efficiency, accuracy and convergency), the 2nd-order HOSPM is a better choice. Therefore, the following analysis will focus on the 2nd-order HOSPM.

C. Correlation length and RMS height

The correlation length is a fundamental quantity that describes a random rough surface. It provides a benchmark for estimating the level of independence between any two points on a random rough surface. If the distance between two points is larger than the correlation length l , the heights of these two points can be approximately regarded as independent. The RMS height h is a fundamental quantity that describes the roughness of a rough surface. The larger the RMS height is, the rougher the surface is. Therefore, the appropriate ranges of RMS heights and correlation lengths in which our method is applicable should be discussed.

Considering the analysis presented in subsection A, the HOSPM will be studied only at 2nd-order in this subsection and next for brevity. The regions of validity with regard to the backscattering and forward scattering angles for the 2nd-order HOSPM are examined based on two sets of simulations, as shown in Fig. 4. Each set consists of 325 different combinations of values of the varies from 0.1 to 2.5 in increments of 0.1 correlation lengths and RMS heights. The value of kl ($0.16\text{m} \leq l \leq 0.40\text{m}$), whereas kh varies from 0.05 to 0.65 in increments of 0.05 ($0.008\text{m} \leq h \leq 0.104\text{m}$).

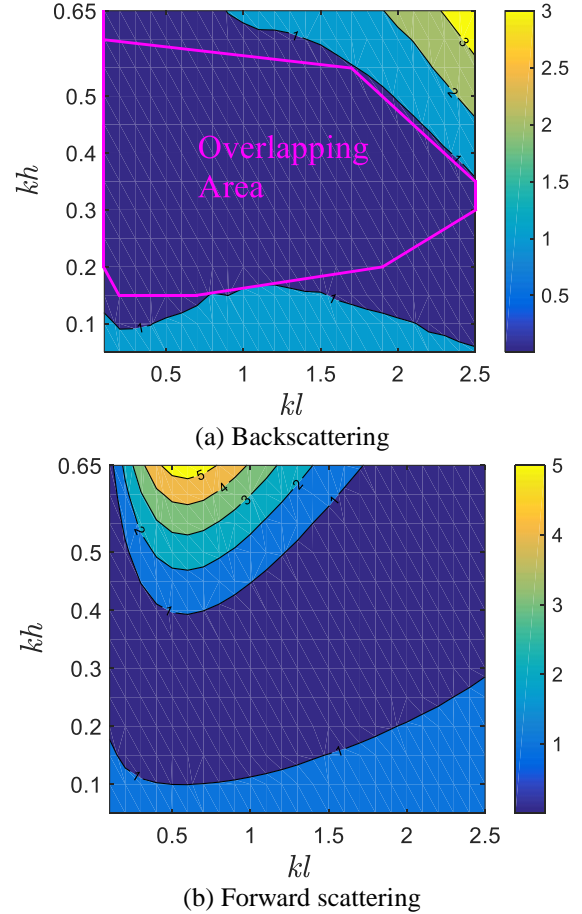


Fig. 4. Contour plot of $|\sigma_{\text{MOM}} - \sigma_{\text{HOSPM2}}|$ for backscattering and forward scattering direction when $\lambda=1\text{m}$, $\theta_i=45^\circ$, $L=25.6\lambda$, $g=\lambda/4$, $N=256$. Both σ_{MOM} and σ_{HOSPM2} are in decibels. The area enclosed by pink lines in (a) is the overlapping area for (a) and (b) under the condition $|\sigma_{\text{MOM}} - \sigma_{\text{HOSPM2}}| \leq 1\text{dB}$.

For the backscattering case, as illustrated in Fig. 4 (a), the 2nd-order HOSPM and the MOM show very good agreement in a broad region where kl spans the domain of the horizontal axis, and kh covers most the area of the figure, leaving only a little space in the upper right corner, where both kl and kh approach maximums.

In the small region near $kl=2.5$ and $kh=0.65$ ($l=0.40\text{m}$ and $h=0.104\text{m}$), the difference between the two methods eventually grows to 3dB, indicating that the 2nd-order HOSPM is not suitable for the backscattering case when the RMS height and correlation length are both large.

For the forward scattering case, as illustrated in Fig. 4 (b), there is a large region in which the difference between the two methods is below 1dB. In this region, the value of kl ranges from 0 to 2.5 ($0 \leq l \leq 0.40\text{m}$), and kh ranges from 0 to 0.65 ($0 \leq h \leq 0.103\text{m}$). The error is approximately 5dB in a small region near $kl=0.6$ and $kh=0.65$ ($l=0.10\text{m}$ and $h=0.103\text{m}$). This small region

should be avoided when the HOSPM is used to estimate forward scattering.

The region enclosed by pink lines in Fig. 4 (a) represents the overlapping region for backscattering and forward scattering, where the condition $|\sigma_{\text{MOM}} - \sigma_{\text{HOSPM}_2}| \leq 1\text{dB}$ is satisfied for both cases. In this region, kl ranges from 0 to 2.5 ($0 \leq l \leq 0.40\text{m}$), and kh ranges from 0.15 to 0.5 ($0.024\text{m} \leq h \leq 0.80\text{m}$). The overlapping area takes up most of the area under discussion. This provides a broad choice of suitable values when scattering data from both the backscattering and forward scattering directions are needed.

Table 3: The backscattering coefficients and forward scattering coefficients of different frequencies

$f(\text{Hz})$	BC(dB)	FC(dB)	$f(\text{Hz})$	BC(dB)	FC(dB)	$f(\text{Hz})$	BC(dB)	FC(dB)
1.0G	-20.27	11.08	15.0G	-19.78	11.08	300G	-20.06	11.1
1.5G	-21.14	11.07	30.0G	-19.89	11.08	333G	-20.37	11.08
3.0G	-20.35	11.06	33.3G	-19.37	11.06	375G	-20.20	11.09
3.3G	-19.95	11.04	37.5G	-19.35	11.12	429G	-19.61	11.10
3.7G	-20.20	11.13	42.9G	-20.37	11.09	500G	-19.83	11.07
4.3G	-20.82	11.13	50.0G	-19.81	11.10	600G	-19.90	11.08
5.0G	-21.32	11.08	60.0G	-20.12	11.09	750G	-20.83	11.11
6.0G	-19.68	11.12	75.0G	-20.13	11.08	1.0T	-19.73	11.04
7.5G	-20.21	11.09	100.0G	-19.51	11.05	1.5T	-19.62	11.09
10.0G	-20.04	11.07	150.0G	-19.71	11.12	3.0T	-19.86	11.07

BC: the abbreviation of backscattering coefficient.

FC: the abbreviation of forward scattering coefficient.

D. Frequency robustness

As discussed above, the 2nd-order HOSPM has been proven to be good for both the backscattering and forward scattering angles. This section will focus on the frequency stability of the BSCs for these two angles. The analysis considers a range of frequencies from 1.0GHz to 3.0THz. A table and a figure are presented to illustrate the analysis. The univariate boxplot introduced by [29] is used to analyze the frequency robustness of the HOSPM, as shown in Fig. 5.

- Table of backscattering and forward scattering coefficients (Table 3). Both the backscattering and forward scattering coefficients are stable for frequencies from 1.0GHz to 3THz. The values of the backscattering coefficients vary only slightly. The difference between the largest and smallest values is less than 2dB. The values vary even less for the forward scattering coefficients, with a difference between the largest and smallest values of no more than 0.1dB.

- Box plot (Fig. 5). This plot visualizes the backscattering and forward scattering coefficients shown in Table 3 for different frequencies. The box plot displays the distributions of the sorted backscattering and forward scattering coefficients, where the observations along the x axis represent the different observation sets and the observations on the y axis represent the values obtained. For both sets, most values are very closely clustered, with no outliers. This plot also yields various statistical summary measures for the data in our sets. For the backscattering coefficients, the: minimum value is -21.14dB, the median is -20.26dB, and the maximum value is -19.65dB. For the forward scattering coefficients, the: minimum value is 11.03dB, the median is 11.09dB, and the maximum value is 11.16dB.

In brief, our method can be applied over a wide range of frequencies with high numerical stability.

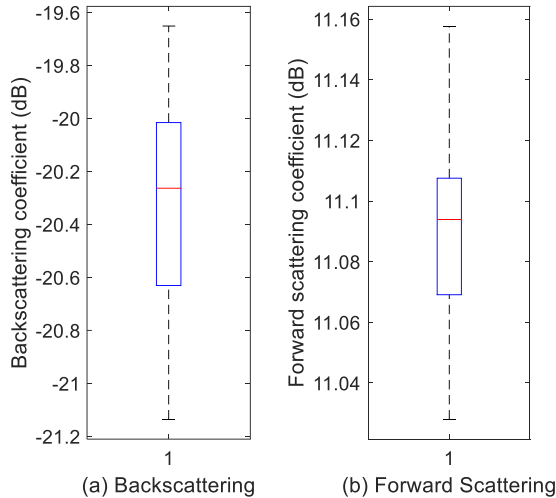


Fig. 5. Boxplot: backscattering and forward scattering coefficients by 2nd-order HOSPM among different frequencies.

V. DISCUSSION

The proposed method provides general explicit closed-form HOSPM expressions of arbitrary orders for solving the problem of the EM fields scattered from 1-D conducting random rough surfaces under TE incidence. The main contributions of this new method are four-fold: first, the surface field is treated as a function of the surface profile, allowing the total field to be expanded in power series form; second, the classic SPM is restricted to series of order two, whereas the applicability of our method extends to arbitrary orders; third, Faà di Bruno's formula is introduced into CEM for the first time to expand a tapered incident wave and its partial derivatives in power series form; and fourth, the obtained mathematical form is simple and easy to program and does not require any mathematical pretreatment.

In the context considered here, our method has been validated from many perspectives.

- In simulation A, the 1st-, 2nd-, 4th- and 8th-order HOSPMs were compared with the numerically exact MOM. The accuracy of the HOSPM at 1st-order and above was verified to be high. The convergence of the HOSPM was discussed with regard to the backscattering and forward scattering angles. The 1st-order form and above are considered to be satisfactory.
- In simulation B, the computational complexities of the 1st-, 2nd-, 3rd-, and 4th-order HOSPMs and the MOM were compared to investigate the efficiency of the proposed method. The results show that the larger the scale of the problem is, the better the HOSPM performs. Considering all factors mentioned above (accuracy, convergence, and time efficiency), the 2nd-order HOSPM applied to the

backscattering and forward scattering angles was selected as a representative pair of cases for further study.

- In simulation C, the regions of validity of the 2nd-order HOSPM with respect to correlation lengths and RMS heights were investigated. It was shown that the HOSPM exhibits high precision and stability over a broad range of correlation lengths and RMS heights.
- In simulation D, the values of the backscattering and forward scattering coefficients were determined for 30 different frequencies. The method was confirmed to be stable over a broad frequency spectrum ranging from 1.0 GHz to 3.0 THz.

VI. CONCLUSION

We can conclude that HOSPM is a method with a rigorous mathematical form, high accuracy, high efficiency and greater suitability for application to a wide variety of different rough surfaces and different frequencies. Moreover, this model can further be used to study radar echoes from dynamic ocean surfaces and various inclusions in studies of composite EM scattering from targets and sea backgrounds. A fast and accurate forward model is necessary to ensure a successful inversion process. Therefore, our method is necessary and important for many inversion scenarios. It can be used in the retrievals of subsurface soil moisture measurements, in planetary exploration, and in the analysis of other natural scenes and can also serve as an important tool for radar system design. Hence, our future work will focus on higher-order solutions for dielectric or multilayer rough surfaces with an arbitrary number of rough interfaces under both TE and TM incidence.

ACKNOWLEDGMENT

This work is partly supported by National Nature Science Foundation of China [grant number 61601356], Shaanxi National Science Foundation [grant number 2016JQ6079] and Basic Scientific Research Foundation of Xidian University [JB180220/20101185311]. The authors would like to thank the reviewers for their valuable comments and constructive suggestions.

APPENDIX: EXPRESSIONS FOR THE PARTIAL DERIVATIVES OF A TAPERED INCIDENT WAVE

The computation of the derivatives of $e^{f(x)}$ is both useful and ubiquitous in analysis. Faà di Bruno's formula, named after Francesco Faà di Bruno, is a mathematical identity for generalizing this problem.

Because a Thorsos tapered incident wave can be expressed as,

$$\psi_i(\mathbf{r}) = e^{z(\mathbf{r})}, \quad (31)$$

where

$$\chi(\mathbf{r}) = ik(x \sin \theta_i - z \cos \theta_i)(1 + w(\mathbf{r})) - \frac{(x + z \tan \theta_i)^2}{g^2}, \quad (32)$$

the series expansion of this tapered incident wave can be derived using Faà di Bruno's formula[30]. This expansion has the form:

$$\psi_i^{(m)}(\mathbf{r}) = \sum_{k=1}^m \psi_i^{(k)}(\mathbf{r}) B_{m,k}(\chi'(\mathbf{r}), \chi''(\mathbf{r}), \dots, \chi^{(m)}(\mathbf{r})). \quad (33)$$

Here, the $B_{m,k}(\chi'(\mathbf{r}), \chi''(\mathbf{r}), \dots, \chi^{(m)}(\mathbf{r}))$ are the Bell polynomials, which have the form,

$$B_{m,k}(\chi'(\mathbf{r}), \chi''(\mathbf{r}), \dots, \chi^{(m)}(\mathbf{r})) = \sum_{\substack{a_1 + 2a_2 + \dots + ma_m \\ a_1 + a_2 + \dots + a_m = k}} \frac{n! [\chi']^{a_1} [\chi'']^{a_2} \dots [\chi^{(m)}]^{a_m}}{a_1! (1!)^{a_1} a_2! (2!)^{a_2} \dots a_m! (m!)^{a_m}}, \quad (34)$$

where χ' , χ'' and $\chi^{(m)}$ are used as abbreviations for $\chi'(\mathbf{r})$, $\chi''(\mathbf{r})$ and $\chi^{(m)}(\mathbf{r})$, respectively, and a_1, a_2, \dots and a_m are all integers greater than or equal to zero. The Bell polynomials also satisfy the following relation ($m \geq 1$):

$$kB_{m,k} = \sum_{l=k-1}^{m-1} \binom{m}{l} \chi^{(m-l)}(\mathbf{r}) B_{m,k-1}, \quad (35)$$

where $B_{m,k}$ and $B_{m,k-1}$ are used as abbreviations for $B_{m,k}(\chi'(\mathbf{r}), \chi''(\mathbf{r}), \dots, \chi^{(m)}(\mathbf{r}))$ and $B_{m,k-1}(\chi'(\mathbf{r}), \chi''(\mathbf{r}), \dots, \chi^{(m)}(\mathbf{r}))$, respectively. This relation is useful for programming the necessary calculations.

REFERENCES

- [1] T. Wang and C. M. Tong, "An improved facet-based TSM for electromagnetic scattering from ocean surface," *IEEE Geosci. Remote Sens. Lett.*, vol. 15, no. 5, pp. 644-648, 2018.
- [2] Y. Wang, K. S. Chen, L. Tsang, and L. Yu, "Depolarized backscattering of rough surface by AIEM model," *IEEE J. Sel. Top. Appl. Earth Observ. Remote Sens.*, vol. 10, no.~11, pp. 4740-4752, 2017.
- [3] S. El-Bah, R. Dusséaux, and S. Afifi, "Some statistical and spatial properties of signal scattering by 2-D slightly rough random surfaces," *IEEE Trans. Antennas Propag.*, vol. 64, no. 2, pp. 721-729, 2016.
- [4] T. H. Liao, L. Tsang, S. W. Huang, N. Niamsuwan, S. Jaruwatanadilok, and S. B. Kim, "Copolarized and cross-polarized backscattering from random rough soil surfaces from L-band to Ku-band using numerical solutions of Maxwell's equations with near-field precondition," *IEEE Trans. Geosci. Remote Sensing*, vol. 54, no. 2, pp. 651-662, 2016.
- [5] C. A. Guérin and J. T. Johnson, "Cross-polarized backscattering under the second-order small-slope approximation," *IEEE Trans. Geosci. Remote Sensing*, vol. 53, no. 11, pp. 6308-6314, 2015.
- [6] A. Torabi, S. A. Zekavat, and K. Sarabandi, "Wideband directional channel characterization for multiuser MIMO systems over a random rough dielectric ground," *IEEE Trans. Wirel. Commun.*, vol. 15, no. 5, pp. 3103-3113, 2016.
- [7] E. N. Grossman, N. Popovic, and R. A. Chamberlin, "Submillimeter wavelength scattering from random rough surfaces," *IEEE THz. Sci. Technol.*, vol. 7, no. 5, pp. 546-562, 2017.
- [8] K. Li, L. X. Guo, and J. Li, "Investigation of bistatic scattering of a 2-D target coated with double negative materials above 1-D random rough surface by FDTD method," *Proc. Cross Strait Quad-Regional Radio Wireless Conf.*, Chengdu, Sichuan, pp. 435-438, 2013.
- [9] S. Sung, N. Bajwa, W. S. Grundfest, and Z. D. Taylor, "Exploration of the Rayleigh roughness in THz medical imaging," *Proc. Int. Conf. Infrared, Millimeter and THz Waves*, Hong Kong, 2015.
- [10] C. Yin, Y. L. Geng, Y. J. Pan, and H. Y. Jin, "Fast algorithm for rough surface scene simulation in passive millimeter wave imaging," *IEEE Access*, vol.~6, pp. 25051-25059, 2018.
- [11] R. Wang, L. X. Guo, and Z. B. Zhang, "Scattering from contaminated rough sea surface by iterative physical optics model," *IEEE Geosci. Remote Sens. Lett.*, vol. 13, no. 4, pp. 500-504, 2016.
- [12] H. Zamani, A. Tavakoli, and M. Dehmollaian, "Scattering by a dielectric sphere buried in a half-space with a slightly rough interface," *IEEE Trans. Antennas Propag.*, vol. 66, no. 1, pp. 347-359, 2018.
- [13] S. Afifi, and R. Dusséaux, "Scattering from 2-D perfect electromagnetic conductor rough surface: analysis with the small perturbation method and the small-slope approximation," *IEEE Trans. Antennas Propag.*, vol.~66, no.~1, pp. 340-346, 2017.
- [14] H. Zamani, A. Tavakoli, and M. Dehmollaian, "Scattering from two rough surfaces with inhomogeneous dielectric profiles," *IEEE Trans. Antennas Propag.*, vol.~63, no.~12, pp. 5753-5766, 2015.
- [15] L. Tsang, J. A. Kong, and K. H. Ding, *Scattering of Electromagnetic Waves: Theories and Applications*. John Wiley & Sons, New York, 2000.
- [16] O. Gilgert, C. Deumie, and C. Amra, "Angle-resolved ellipsometry of scattering patterns from arbitrary surfaces and bulks," *Opt. Express*, vol. 13, no. 7, pp. 2403-2418, 2005.

- [17] J. E. Elson, "Infrared light scattering from surfaces covered with multiple dielectric overlayers," *Appl. Optics*, vol. 16, no. 1, pp. 2872-2881, 1977.
- [18] C. D. Jones and D. R. Jackson, "Infrared light scattering from surfaces covered with multiple dielectric overlayers," *IEEE J. Oceanic ENG.*, vol. 26, no. 1, pp. 84-93, 2001.
- [19] S. O. Rice, "Reflection of electromagnetic waves from slightly rough surfaces," *Commun. Pure Appl. Math.*, vol. 4, pp. 351-378, 1951.
- [20] J. T. Johnson, "Third-order small-perturbation method for scattering from dielectric rough surfaces," *J. Opt. Soc. Am. A-Opt. Image Sci. Vis.*, vol. 16, no. 11, pp. 2720-2736, 1999.
- [21] M. A. Demir, J. T. Johnson, and T. J. Zajdel, "A study of the fourth-order small perturbation method for scattering from two-layer rough surfaces," *IEEE Trans. Geosci. Remote Sensing*, vol. 50, no. 9, pp. 3374-3382, 2012.
- [22] J. A. Kong, *Electromagnetic Wave Theory*. EMW Publishing, Cambridge, 2008.
- [23] E. I. Thorsos, "The validity of the Kirchhoff approximation for rough surface scattering using a Gaussian roughness spectrum," *J. Acoust. Soc. Am.*, vol. 83, no. 11, pp. 78-92, 1988.
- [24] L. Tsang, J. A. Kong, and K. H. Ding, *Scattering of Electromagnetic Waves: Numerical Simulation*. John Wiley & Sons, Inc., New York, 2001.
- [25] H. X. Ye and Y. Q. Jin, "Parameterization of the tapered incident wave for numerical simulation of electromagnetic scattering from rough surface," *IEEE Trans. Antennas Propag.*, vol. 53, no. 3, pp. 1234-1237, 2005.
- [26] J. T. Johnson and R. J. Burkholder, "A study of scattering from an object below a rough surface," *IEEE Trans. Geosci. Remote Sensing*, vol. 42, no. 1, pp. 59-66, 2004.
- [27] J. T. Johnson, "A numerical study of scattering from an object above a rough surface," *IEEE Trans. Antennas Propag.*, vol. 50, no. 10, pp. 1361-1367, 2002.
- [28] G. Macelloni, G. Nesti, P. Pampaloni, and S. Sigismondi, "Experimental validation of surface scattering and emission models," *IEEE Trans. Geosci. Remote Sensing*, vol. 38, no. 1, pp. 459-469, 2000.
- [29] J. W. Tukey, "Mathematics and the picturing of data," *Proc. Int. Congress Mathematicians*, Vancouver, pp. 523-532, 1974.
- [30] K. Drakakis, "On a closed formula for the derivatives of $e^{f(x)}$ and related financial applications," *International Mathematical Forum*, vol. 4, no. 9, pp. 401-407, 2009.



Qing Wang was born Shaanxi, China, in 1984. She received the B.Eng. degree in Measuring and Control Technology and Instrumentations from Xidian University, China, in 2006 and Ph.D. degree in Electromagnetic Field and Microwave Technology from Xidian University, China, in 2012. From 2009 to 2011, she was a visiting student in Clemson University, USA.

She is currently an Assistant Professor with the School of Electronic Engineering, Xidian University, Xi'an. Her research interests include computational electromagnetics and millimeter wave technology.



Chen Lin was born in Jiangsu, China, in 1982. He received the B.Eng. Degree in Measuring and Control Technology and Instrumentations from Xidian University, China, in 2006 and Ph.D. degree in Electromagnetic Field and Microwave Technology from Xidian University, China, in 2011.

He is currently a Senior Engineer with Yangzhou Marine Electronic Institute. His research interest contains radar system analysis and engineering, microwave engineering and electronically scanned arrays.



Zhen-Ya Lei was born in Shaanxi, China, in 1960. He received the B.Eng. degree in Computer Science from Xidian University, China, in 1981 and M.E. degree in Electromagnetic Field and Microwave Technology from Xidian University, China, in 1998. He was a visiting scholar in Ohio State University, U.S. in 2016.

He is currently a Professor with the School of Electronic Engineering, Xidian University, Xi'an. His research interest contains microwave circuits and microwave engineering, Rf/microwave transmitter and the receiver, antenna, system-level EM field analysis, target characteristics and stealth design.



Jian-Qiang Hou received the B.Eng. degree in Electromagnetic Field and Microwave Technology from Xidian University, China, in 1999, M.E. degree in Electromagnetic Field and Microwave Technology from Xidian University, China, in 2004 and Ph.D. degree in

Electromagnetic Field and Microwave Technology from Xidian University, China, in 2012.

He is currently an Associate Professor with the School of Electronic Engineering, Xidian University, Xi'an. His research interest contains millimeter-wave circuits and systems and modeling and design of microwave devices.



Lei Li was born in 1980. He received the B.Eng. degree in Electronic Engineering from Shenyang Aerospace University, China, in 2001, M.E. degree in Electromagnetic Field and Microwave Technology from Xidian University, China, in 2005 and Ph.D. degree in

Electromagnetic Field and Microwave Technology from Xidian University, China, in 2007. From 2015 to 2016, he was a visiting scholar in University of Montreal, Canada.

He is currently an Associate Professor with the School of Electronic Engineering, Xidian University, Xi'an. His research interest contains substrate integrated waveguide and target characteristics.